UNIVERSITÀ DEGLI STUDI DI TORINO

B3LYP Periodic Study of the Physico-Chemical Properties of the Non-Polar (010) Mg-Pure and Fe-Containing Olivine Surfaces

Javier Navarro-Ruiz,[a] Piero Ugliengo,[b] Albert Rimola[a,*] and Mariona Sodupe[a,*]

[a] Departament de Química, Universitat Autònoma de Barcelona, 08193 Bellaterra,

Spain

[b] Dipartamento Chimica and NIS Centre , Università degli Studi di Torino, 10125

Torino (Italy)

Corresponding authors:

E-mail: albert.rimola@uab.cat; Phone number: 0034-93-5812173

E-mail: mariona.sodupe@uab.cat; Phone number: 0034-93-5813031

Keywords:

(Mg,Fe)-olivines, periodic DFT, IR spectrum, reflectance spectrum, dust particles

Abstract

B3LYP periodic simulations have been carried out to study some physico-chemical properties of the bulk structures and the corresponding non-polar (010) surfaces of Mg-pure and Fe-containing olivine systems; i.e, Mg_2SiO_4 (Fo) and $Mg_{1.5}Fe_{0.5}SiO_4$ (Fo$_{75}$). A detailed structural analysis of the (010) Fo and Fo$_{75}$ surface models shows the presence of coordinatively unsaturated metal cations (Mg^{2+} and Fe^{2+}, respectively) with shorter metal-O distances compared to the bulk ones. Energetic analysis devoted to the Fe^{2+} electronic spin configuration and to the ion position in the surfaces reveals that Fe^{2+} in its quintet state and placed at the outermost positions of the slab constitutes the most stable Fe-containing surface, which is related to the higher stability of high spin states when Fe^{2+} is coordinatively unsaturated. Comparison of the simulated IR and the corresponding reflectance spectra indicates that Fe^{2+} substitution induces an overall bathochromic shift of the spectra due to the larger mass of Fe compared to Mg cation. In contrast, the IR spectra of the surfaces are shifted to upper values and exhibit more bands compared to the corresponding bulk systems due to the shorter metal-O distances given in the coordinatively unsaturated metals and to symmetry reduction which brings non-equivalent motions between the outermost and the internal modes, respectively.

Introduction

Olivines are silicate solid solutions with general formula $Mg_{2x}Fe_{(2-2x)}SiO_4$ (x = 0 − 1) and are one of the most abundant silicate groups in the Earth's upper mantle. Crystalline olivines present an orthorhombic structure with space group *Pbnm* and are characterized to have $[SiO4]^{4-}$ tetrahedra linked by the divalent cations. Their magnesium and iron end members are forsterite (Mg_2SiO_4) and fayalite (Fe_2SiO_4). The interest for investigating olivines is not only due to their prominence as common rock-

forming minerals but also because olivinic dust grains are ubiquitously present throughout interstellar and circumstellar media.[1-3] An important chemical role of cosmic dust particles is, like in heterogeneous catalysis, to accelerate certain astrochemical reactions by orders of magnitude when occurring at their surfaces.[4, 5] The presence of dust grains is especially important for the synthesis of molecules that otherwise would be impossible to form via simple gas-phase reactions, such as H_2[6, 7] and H_2O,[8] two of the most relevant molecules in the Universe. On Earth, these silicate groups are mostly found in a crystalline state whereas cosmic olivines are mainly present as amorphous materials,[3] although crystalline forms have also been detected.[9] Both on Earth and in space, crystalline olivines appear to be richer in magnesium than in iron.[9, 10]

Atomic-scale simulations of solid state surfaces are useful techniques to understand their physico-chemical properties, as they provide structural atomistic details (e.g., the presence and nature of surface defects), one-electron properties (e.g., charge distribution, electrostatic potentials, spin densities) or spectroscopic properties, (e.g, vibrational features and infra-red signatures). Forsterite surfaces are by far the most studied olivine surfaces with different atomistic simulation techniques;[11-27] i.e., by means of a periodic treatments or cluster model approaches using classical shell-ion model potentials and density functional methods. Moreover, most of these studies include the interaction with H[14-18] and H_2O[19-27] to evaluate the adsorption features. The large number of studies on forsterite contrasts with the limited works focused on Fe-containing olivine surfaces, the available theoretical works being limited to the bulk and the (010) surface of fayalite.[28-31] This lack of theoretical studies is partly due to the large compositional variability in these minerals that can tolerate various isomorphic substitutions and to the fact that the treatment of Fe-containing minerals bears additional difficulties due to the possible presence of strong correlations effects.

Therefore, the physico-chemical properties of Fe-bearing olivine surfaces (and in a more extent, of Fe-bearing minerals) are poorly understood. Understanding these systems is of significant importance because they serve as an important source for electrons in redox reactions in various geochemical environments.[32-35] Moreover, the change of the Fe oxidation state has a profound impact on the electronic structure of the surfaces of these minerals, such as in their adsorption properties and chemical activity. Several theoretical works have been devoted to understand the redox activity of the $Fe^{2+/3+}$ pair in different clays and minerals.[36-40]

The aim of the present work is to provide, based on ab-initio electronic structure calculations, a detailed description of different physico-chemical features of the bulk and (010) surfaces (the main cleavage crystallographic plane of forsterite) of Mg_2SiO_4 and $Mg_{1.5}Fe_{0.5}SiO_4$ (25% of Fe^{2+} substitution), this latter being considered as a paradigmatic case for the Fe-containing olivine surfaces. In particular, analysis of the surface structures, electronic properties (electrostatic potentials, spin densities, Fe^{2+} electronic states), vibrational (IR spectra) and dielectric (reflectance spectra) properties is presented. Special attention to the differences between Mg-pure and Fe-containing surfaces is also addressed.

Computational Details

All periodic calculations have been performed with the ab initio CRYSTAL09 code.[41] This code implements the Hartree−Fock and Kohn−Sham self-consistent field method based on localized Gaussian Type Orbitals (GTO) for periodic systems.[42] Surface models computed by CRYSTAL09 are true 2D systems, at variance to plane

wave-based codes, in which the slab is artificially replicated through infinity also in the direction perpendicular to the slab by including a large amount of empty space.

The multielectron wave function is described by linear combination of crystalline orbitals, which in turn are expanded in terms of GTO basis sets. Specifically, oxygen, magnesium, silicon and iron were described by (8s)-(411sp)-(1d), (8s)-(511sp)-(1d), (8s)-(6311sp)-(1d), and (8s)-(64111sp)-(1d) contractions, respectively; these basis functions were already used in previous works focused on the forsterite[43-45] and fayalite[30] bulk properties.

All the SCF calculations and geometry optimizations were performed with the B3LYP density functional method.[46, 47] Geometry optimizations of the forsterite bulk systems have been performed in *Pbnm* space symmetry, whereas of the Fe-containing bulks structures and for the surface models in *P1* group symmetry (no symmetry), in order to ensure the maximum degrees of freedom during the optimization. Both lattice constants and internal coordinates have been simultaneously optimized within the same run, using analytical gradients and upgrading the numerical Hessian with the Broyden−Fletcher−Goldfarb−Shanno (BFGS) algorithm.[48-51] Default values of the tolerances that control the Coulomb (6 6 6 6) and exchange (14) series have been adopted. This means that when the overlap between two atomic orbitals is smaller than 10^{-6} (for Coulomb) and 10^{-14} (for exchange) the integral is either approximated or disregarded.[41] The Hamiltonian matrix has been diagonalized[52] in 20 reciprocal lattice points (k points) to sample the Brillouin zone, corresponding to a shrinking factor of 6.[41] Open-shell calculations were based on an unrestricted formalism. Electron spin densities on the atoms have been obtained by using the Mulliken population analysis.

Phonon frequencies of the considered systems have been calculated as the eigenvalues obtained by diagonalizing the mass-weighted Hessian matrix at Γ point

(point k = 0 in the first Brillouin zone, called the central zone). The mass-weighted Hessian matrix was obtained by numerical differentiation (central-difference formula) of the analytical first energy derivatives, calculated at geometries obtained by displacing, in turn, each of the 3N equilibrium nuclear coordinates by a small amount, u= 0.003 Å. We refer to this work[53] for a complete discussion of the computational conditions and other numerical aspects concerning the calculation of the vibrational frequencies at the Γ point. The value of the infrared intensity for each normal mode was also computed via the dipole moment variation along the normal mode adopting the set of localized Wannier functions.[54-56]

Reflectance spectra (R(ν)) of 3D-periodic systems can be simulated with CRYSTAL09 by combining different ingredients available in the code: i) calculation of the vibrational modes, their corresponding intensities and separation of the transverse and longitudinal optical (TO and LO, respectively) modes;[53, 57] ii) calculation of the high frequency dielectric tensor (ε_∞)[58-61] contributing to the frequency-dependent complex dielectric function ($\varepsilon(\nu)$); and iii) calculation of the mass-weighted effective mode Born charges.[62-64] Reflectance spectra of several crystalline mineral systems have successfully been simulated with CRYSTAL09[30, 44, 45, 65-67] and the interested reader can find all details there.

Results and discussion

For the sake of brevity, the forsterite (Mg_2SiO_4)-related systems will be hereafter referred to Fo and the Fe-containing ($Mg_{1.5}Fe_{0.5}SiO_4$) ones to Fo_{75}. This section is organized as follows. First, results related to the structures and to some energy-related features of both the bulk systems and the (010) surfaces of Fo and Fo_{75} are shown.

Then, analyses of the electrostatic potential maps of the very same surfaces and of the spin density distribution of the Fo_{75} are provided. Subsequently, the simulated infrared and reflectance spectra of these systems are shown, paying special emphasis to the changes given by the presence of Fe.

Structure and energy-related features. The bulk crystal structure of Fo and Fo_{75} is very similar (see Figure 1). They are made up by distorted SiO_4 tetrahedra and MgO_6/FeO_6 octahedra, in which the tetrahedral and the octahedra share the vertices. Half of the available octahedral voids are occupied by the divalent cations. In Fo there are two symmetry-independent Mg atoms, named Mg1 and Mg2.[68] The Mg1-centered octahedra share edges forming rods parallel to the crystallographic c axis, and the Mg2 octahedra are laterally linked to these rods through the corresponding edges. A substitution of half of Mg2 by Fe the Fo_{75}^{M2} structure is obtained (see Figure 1b), whereas half of Mg1 by Fe yields the Fo_{75}^{M1} one (see Figure 1c). It is worth mentioning that different studies[69-71] indicate that the Fe-containing solid solutions are more stable in the high-spin state than in the low-spin one at normal conditions, and accordingly the bulk Fo_{75}^{M2} and Fo_{75}^{M1} systems have been computed in this high-spin state (i.e., each Fe^{2+} cation (d^6) in a quintet electronic state).

The optimized structural parameters of the bulk structure of Fo (Table 1) are in good agreement with experiments. As already reported,[43] calculated cell parameters are slightly overestimated (giving a volume variation of 2.2%) and the experimental Si–O and Mg–O distances are well reproduced, the largest differences being given in the Mg2-O distances (0.024 Å larger, at the most). The calculated equilibrium geometries of Fo_{75}^{M2} and Fo_{75}^{M1} are also given in Table 1. Cell parameters are larger than those of Fo because of the larger ionic radius of Fe^{2+} than Mg^{2+} (0.78 and 0.72 Å, respectively), and accordingly the volume of the two iron containing systems is larger as well. The

presence of Fe (irrespective of its position) slightly affects the Mg–O distances by increasing their values compared to the Fo ones, whereas the Si–O distances are in both systems very similar to those of Fo.

The large variability of oxygen sub-lattice in Fo results in a complex set of crystal planes. For instance, there are already 7 different planes characterized by the smallest Miller indexes (i.e., ({100}{010}, {001}, {110}, {101}, {011}, {111} crystal forms) whose modelling is rather difficult, since electroneutrality should be enforced by rather complex chemical reconstruction. Normally, slab models are modelled by cutting out the bulk crystal at the Mg-O bonds rather than the Si-O ones to keep the SiO_4 units intact. Moreover, both polar and non-polar surface slabs can be obtained, depending on the edge layers and the thickness of the slab model. In this work, the non-polar (010) forsterite surface (hereafter referred as Fo^{surf}) has been studied (shown in Figure 2a), since it is the major cleavage plane of Fo and, according to previous calculations, the most stable surface in dry conditions.[11, 19, 21] This non-polar surface is terminated by edge-layers containing both M2 magnesium ions and oxygen atoms, in which Mg^{2+} cations are unsaturated centres coordinated by 3 O atoms. The polar (010) surface (not considered in this wok) is terminated by a half vacant layer of M1 magnesium ions.[11] For the Fe-containing systems, three different slab models have been designed from the two initial bulk structures; i.e., Fo_{75}^{top} and the Fo_{75}^{int} surfaces from Fo_{75}^{M2} ; and Fo_{75}^{mid} from Fo_{75}^{M1}. Fo_{75}^{top} exhibits the Fe^{2+} ions at the outermost positions of the edge-layers of the slab model (see Figure 2b) and, similarly to the analogous Mg^{2+} ions in Fo^{surf}, are coordinatively unsaturated centres. In Fo_{75}^{mid}, the Fe ions are placed in the mid-regions of the slab, see Figure 2c), whereas in Fo_{75}^{int} they are in the innermost regions (see Figure 2d). For these surfaces, the atomic integrated spin density has been evaluated by computing both the quintet, triplet and singlet states per Fe^{2+} ions. Considering that a

unit cell contains two Fe^{2+} cations, the overall spin multiplicity for the unit cell is, therefore, nonaplet, quintet and singlet, respectively.

The calculated equilibrium interatomic distances of Fo and Fo_{75} (010) surfaces are given in Table 2 and the optimized cell parameters in Table 3. The calculated slab models are almost bulk-terminated surfaces with slight undulating surface topologies. This is in agreement with the experimental study of Hochella,[72] in which the forsteritic {010} crystal form was found to be 1x1 surface unit cells with small relaxations using low energy electron diffraction. The internal Si-O and metal-oxygen distances are very similar to those present in the respective bulk structures, demonstrating the low reconstruction suffered by these surfaces. However, the outermost Mg-O and Fe-O (for $Fo_{75}{}^{top}$) distances are significantly shorter (about 0.2 Å) because these metal ions are coordinatively unsaturated. Moreover, the outermost Si-O distances are also shorter (about 0.025 Å) than the internal ones. Consequently, the lattice parameters of the surfaces are somewhat shorter compared to the corresponding bulk values (i.e., about 1% for a and 2.3 % for c). On the other hand, for Fo_{75} surfaces, it is observed that the Fe-O distances are larger for Fe^{2+} in the quintet state than in the triplet and the singlet states, and accordingly surface areas decrease with the spin multiplicity. This is due to the larger electronic repulsion between the Fe^{2+} 3d electrons and O^{2-} in the quintet state than in the triplet and singlet ones.

The relative stability of Fo_{75} (010) surfaces has been calculated considering the electronic state and the position of the Fe^{2+} cations (Figure 3). The most stable surface concerns the Fe^{2+} ions placed at the outermost positions in a quintet spin state (i.e., hereafter referred as $Fo_{75}{}^{top}$(qt)). Moreover, for the three surfaces, the relative stability of the three spin states considered follow the order qt > tp > sg, i.e., the most stable Fe^{2+} spin configuration is the quintet high spin state, in consistency with what is known

for bulk solid solutions. Noteworthy, for the Fe^{2+} in the quintet and triplet spin states, Fo_{75}^{top} surfaces are more stable than Fo_{75}^{mid} and Fo_{75}^{int}, whereas for the singlet state, Fo_{75}^{mid} becomes the most stable surface, in agreement with the fact that saturated coordination environments stabilize low spin versus high spin states. Note that saturated environments induce a larger splitting of 3d orbitals.

The surface energy of Fo^{surf} has been calculated to be 1.16 Jm^{-2}, implying that the cleavage of the bulk crystal to create this surface is not a highly energetic process. Its stability may be due to the formation of O–Mg–O bridges on the surface, similar to O–Si–O and O–Na–O bridges, which were found to stabilise α-quartz-based surfaces.[73] The presence of alternating O-Si-O and O-Mg-O surface bridge groups gives rise to a surface energy similar to that for the (010) MgO surface (1.20 Jm^{-2}). The calculated surface energy of $Fo_{75}^{top}(qt)$, is 0.87 Jm^{-2}, 0.29 Jm^{-2} lower than Fo^{surf}, meaning that less energy is needed to cut the corresponding bulk system and that the $Fo_{75}^{top}(qt)$ is expected to be less reactive than Fo^{surf}. This lower surface energy of $Fo_{75}^{top}(qt)$ is associated to the high spin of Fe^{2+}, (note that triplet and singlet states exhibit higher surface energies) since the loss of Fe-O electrostatic interactions in $Fo_{75}^{top}(qt)$ is partly compensated by a larger decrease of electron repulsion between Fe^{2+} 3d electrons and O^{2-} in this spin state quintet state upon generating the surface.

Electrostatic Potentials and Spin Densities. Electrostatic potential maps (EPMs) show regions of negative and positive potentials and provide clues about the most favourable adsorption sites and of the driving forces involved. Figure 4a and 4b shows the B3LYP-EPMs for Fo^{surf} and $Fo_{75}^{top}(qt)$ on a surface enclosing 90% of the electron density. Both EPMs show prominent positive and negative valued regions, which are associated to the outermost Mg/Fe and O surface atoms, respectively. This suggests that Mg/Fe atoms are the best candidates to interact with electron donor atoms

and surface O atoms for H-bonding interactions and electrophilic molecules. It is worth pointing out that these two well-defined potential regions are less pronounced in the $Fo_{75}^{top}(qt)$ surface, suggesting that favourable electrostatic interactions are expected to be larger in Fo^{surf} rather than in $Fo_{75}^{top}(qt)$. Net charges obtained by a Mulliken population analysis confirms this trend as they are found to be $+1.60|e|$ and $-1.22\ |e|$ for Mg and O, respectively, in Fo^{surf} and $+1.40|e|$ and $-1.19|e|$ for Fe and O, respectively, in $Fo_{75}^{top}(qt)$.

For the case of $Fo_{75}^{top}(qt)$, the spin density features have also been analysed through its spin density map (Figure 4c), which shows the spin localization at the surface atoms. The map clearly shows that the spin of $Fo_{75}^{top}(qt)$ lies mainly at the Fe^{2+} cations, in line with the calculated Mulliken atomic integrated spin density for the Fe atom of $+3.7|e|$ (out of $4|e|$), and about $+0.15|e|$ of the neighboring O atoms. This means that, in addition to establish electrostatic interactions with electron donor atoms, Fe^{2+} sites will be active with respect to adsorbed radical species.

Infrared and Reflectance Properties. Olivines have an orthorhombic structure and present 28 atoms in the unit cell (four formula units per cell), giving rise to 84 vibrational modes (35 IR active modes, 36 Raman active modes, 10 inactive modes and 3 modes to rigid translations). Vibrational modes in silicates are usually classified in two main categories; i) the internal modes (I), which include the stretching and bending vibrations of the SiO_4 tetrahedra; and ii) the external modes (E), which include rotations and translations of the SiO_4 tetrahedra and translations of the metal cations. In previous works,[74-80] mode classification and band assignments of olivinic crystals have exhaustively been discussed by means of infrared, Raman and reflectance spectroscopic measurements. In this part, we focus our attention on the most important IR active

modes for Fo, Fo_{75}^{M2}, Fo^{surf}, and $Fo_{75}^{top}(qt)$ in order to evaluate the different spectral signatures between the bulk and the surfaces and due to the presence of Fe^{2+}.

Table 4 report the comparison between the B3LYP vibrations and the experimental ones for Fo. Here, the comparison with the experimental values gives a range of shifts since the simulated IR bands are due to vibrational active modes of similar wavenumber. As already described,[43] B3LYP frequencies reproduce very well the experimental values, with a mean average of 4.82 cm^{-1} and a largest deviation of 9 cm^{-1}. Remarkably, the largest deviations are associated to the SiO4 bending modes.

Figure 5 shows the comparison between the calculated IR spectra of bulk Fo and Fo_{75}^{M2}. Both systems present 8 common vibrational frequencies in the 200 - 1000 cm^{-1} range. They are due to the translation of the metal cations, the rotation of $[SiO_4]$ and the bending and stretching motions of the SiO_4 tetrahedra. Results show that the overall spectra of Fo_{75}^{M2} is shifted to lower values due to the higher mass of the substituting Fe^{2+}. A comparison of the IR spectrum of Fo_{75}^{M2} with that for Fo in which the Mg^{2+} ions that are substituted by Fe^{2+} in Fo_{75}^{M2} have the mass of iron (hence reproducing a mass-analog of Fo_{75}^{M2}) points out that the shifts are mainly due to the higher mass of Fe^{2+} (see Figure S1 of ESI). This bathochromic shift is significantly important in those bands where Fe^{2+} is involved; that is, those associated to the metal translation (i.e., from 293 to 276 cm^{-1} and from 350 to 280 cm^{-1}) and those associated to modes of SiO_4 bonded to the metal cations (e.g., from 873 to 855 cm^{-1}). This is in agreement with the experimental measurements[81] and theoretical results[30] that compare the IR features of forsterite with fayalite. The very same difference is given when comparing the IR spectra of the Fo^{surf} surface with the $Fo_{75}^{top}(qt)$ one (see Figure S2 of ESI); that is, the latter spectrum is globally bathochromic shifted.

A comparison of the IR spectra between the bulk structures and the corresponding (010) surfaces (Fo vs Fo^{surf} and Fo_{75}^{M2} vs $Fo_{75}^{top}(qt)$ presented in Figure 6 and 7, respectively) shows that spectra of the surface slabs have two significant differences compared to the bulk ones: i) they have been shifted to upper values; and ii) they present more bands. The hypsochromic shift related to point i) is probably due to the shorter distances of the outermost Si-O, Mg-O and Fe-O bonds because the metal ions are coordinatively unsaturated centres (vida supra). The presence of more bands in the spectra of the surfaces (point ii)) is due to the splitting of broad bands present in the bulk spectra associated to the vibrations of atoms of the outermost positions of the surfaces. For instance, the peaks at 293 cm^{-1} (Fo) and 276 cm^{-1} (Fo_{75}^{M2}) belonging to the translations of the metal cation split into the bands at 287 and 309 cm^{-1} (Fo^{surf}) and at 279 and 304 cm^{-1} ($Fo_{75}^{top}(qt)$), or the peaks at 873 cm^{-1} (Fo) and 855 cm^{-1} (Fo_{75}^{M2}) split into the bands at 911 and 945 cm^{-1} (Fo^{surf}) and at 892 and 920 cm^{-1} ($Fo_{75}^{top}(qt)$).

As anticipated in the Computational Details section, the reflectance spectrum of a given 3D-periodic system (namely, bulk structures) can be simulated with the CRYSTAL09 code. As mentioned, an important ingredient for the construction of the reflectance curves is the high frequency dielectric constant ε_∞ computed by means of a CPKS scheme. For Fo, the calculated ε_∞ values along the x, y and z directions are provided in Table 5. Differences with respect to the experimental values are negative, the deviations spanning the 7.8 – 9.3% range (see Table 5). The presence of the Fe^{2+} cations in Fo_{75}^{M2} induces a tiny but generalized increase of the ε_∞ values, which is in line with the larger experimental ε_∞ values of pure forsterite compared to pure fayalite (Table 5).

The reflectance spectra of Fo and Fo_{75}^{M2} along the y direction (the normal direction of the (010) plane) are shown in Figure 8. Expectedly, the reflectance

spectrum of Fo_{75}^{M2} is shifted to lower wavenumbers compared to the Fo one in consistency to the higher mass of the substituted iron. Remarkably, such a bathochromic shift was also observed in the comparison of the single-crystal reflectivity of pure Mg_2SiO_4 with the natural $(Mg_{0.86},Fe_{0.14})SiO_4$.[77] Moreover, the presence of the Fe reduces overall the far-infrared reflectivity of olivine compared to pure forsterite, in agreement to the experimental measurements and caused by the larger refractive index of Fe-containing olivines than the Mg-pure ones.

Conclusions

The bulk forsterite (Mg_2SiO_4) and the $Mg_{1.5}Fe_{0.5}SiO_4$ Fe-containing analog (25% of Fe substitution) as well as the corresponding non-polar (010) surfaces have been simulated by means of B3LYP periodic calculations with the CRYSTAL09 code. Their structural features, electronic properties (i.e., electrostatic potentials and spin density distribution) and vibrational features have been analysed in detail. The following points emerge from the present calculations:

-   B3LYP optimized structural parameters reproduce fairly well the crystallographic data for the bulk forsterite, the calculated cell parameters being slightly overestimated and providing a volume variation of about 2%. Fe^{2+} substitution induces an overall enlargement of the bulk structure because of its larger ionic radius. Reconstruction of the surface is minor and mainly corresponds to the shortening of the outermost metal-O bond distances because the metal cations at these positions are coordinatively unsaturated centres.

-   Relative energy calculations and the calculated surface energies for different Fe^{2+}-electronic states indicate that the most stable Fe-containing surfaces have

the metal cations in the quintet state, followed by the triplet and the singlet states. Moreover, limited to the Fe^{2+}-quintet state, those surfaces with the cations placed at the outermost positions of the slab are more stable than those placed in more internal positions.

- The simulated IR spectra of the bulk systems and the corresponding surfaces present bands associated to the translation motion of the metal cations, to the rotation of the SiO_4 tetrahedra and to the bending and stretching modes of the SiO_4 bond angles and lengths, respectively. Comparison of the different IR indicate that: i) Fe^{2+}substitution induces an overall bathochromic shift of the spectra compared to the Mg-pure ones because of the larger atomic mass of Fe; ii) the IR spectra of the surface slab models are shifted to upper values with respect to the corresponding bulk ones as a consequence of the coordinatively unsaturated metal cations present at the outermost positions of the slab models, which sport shorter metal-O distances; and iii) bands present in the IR spectra of the bulk systems split in the respective surface ones because of the different vibrational signatures of the metal and SiO_4 groups present at the slab edge layers. The calculated reflectance spectra for the bulks of forsterite and the Fe-containing olivine also show the bathochromic shift due to iron substitution.

Supporting Information Available

Complete author list for references 2, 41 and 80. Infra-red spectra comparisons not shown in the text. This information is available free of charge via the Internet at http://pubs.acs.org

References

1.   Henning, T., *Astromineralogy*. Springer-Verlag: Berlin, 2010; p 360.
2.   Colangeli, L.; Henning, T.; Brucato, J. R.; Clément, D.; Fabian, D.; Guillois, O.; Huisken, F.; Jäger, C.; Jessberger, E. K.; Jones, A., et al., The Role of Laboratory Experiments in the Characterisation of Silicon–Based Cosmic Material. *Astron. Astrophys. Rev.* **2003,** *11*, 97-152.
3.   Henning, T., Cosmic Silicates. *Annu. Rev. Astron. Astrophys.* **2010,** *48*, 21-46.
4.   Pironello, V.; Krelowski, J.; Manicò, G., *Solid State Astrochemistry*. Kluwer Academic Publisher: Dordrecht, 2003; Vol. 120, p 463.
5.   Duley, W. W.; Williams, D. A., *Interstellar Chemistry*. Academic Press: London, 1984.
6.   Vidali, G.; Roser, J. E.; Ling, L.; Congiu, E.; Manico, G.; Pirronello, V., The Formation of Interstellar Molecules Via Reactions on Dust Grain Surfaces. *Faraday Disc.* **2006,** *133*, 125-135.
7.   Vidali, G., H2 Formation on Interstellar Grains. *Chem. Rev.* **2013,** *113* 8762-8782.
8.   van Dishoeck, E. F.; Herbst, E.; Neufeld, D. A., Interstellar Water Chemistry: From Laboratory to Observations. *Chem. Rev.* **2013,** *113* 9043-9085.
9.   Molster, F.; Kemper, C., Crystalline Silicates. *Space Sci. Rev.* **2005,** *119*, 3-28.
10.   Nesse, W. D., *Introduction to Mineralogy*. Oxford University Press: New York, 2000.
11.   Watson, G. W.; Oliver, P. M.; Parker, S. C., Computer Simulation of the Structure and Stability of Forsterite Surfaces. *Phys. Chem. Miner.* **1997,** *25*, 70-78.
12.   Reber, A. C.; Paranthaman, S.; Clayborne, P. A.; Khanna, S. N.; Castleman, A. W., From SiO Molecules to Silicates in Circumstellar Space: Atomic Structures,

Growth Patterns, and Optical Signatures of SinOm Clusters. *ACS Nano* **2008,** *2*, 1729-1737.

13.   Goumans, T. P. M.; Bromley, S. T., Efficient Nucleation of Stardust Silicates Via Heteromolecular Homogeneous Condensation. *Mon. Not. R. Astron. Soc.* **2012,** *420*, 3344-3349.

14.   Goumans, T. P. M.; Richard, C.; Catlow, A.; Brown, W. A., Formation of H2 on an Olivine Surface: A Computational Study. *Mon. Not. R. Astron. Soc.* **2009,** *393*, 1403-1407.

15.   Goumans, T. P. M.; Bromley, S. T., Hydrogen and Oxygen Adsorption on a Nanosilicate – A Quantum Chemical Study. *Mon. Not. R. Astron. Soc.* **2011,** *414*, 1285-1291.

16.   Garcia-Gil, S.; Teillet-Billy, D.; Rougeau, N.; Sidis, V., H Atom Adsorption on a Silicate Surface: The (010) Surface of Forsterite. *J. Phys. Chem. C* **2013,** *117*, 12612-12621.

17.   Kerkeni, B.; Bromley, S. T., Competing Mechanisms of Catalytic H2 Formation and Dissociation on Ultrasmall Silicate Nanocluster Dust Grains. *Mon. Not. R. Astron. Soc.* **2013,** *435*, 1486-1492.

18.   Downing, C. A.; Ahmady, B.; Catlow, C. R. A.; de Leeuw, N. H., The Interaction of Hydrogen with the {010} Surfaces of Mg and Fe Olivine as Models for Interstellar Dust Grains: A Density Functional Theory Study. *Phil. Trans. R. Soc. A* **2013,** *371*, 20110592.

19.   de Leeuw, N. H.; Parker, S. C.; Catlow, C. R. A.; Price, G. D., Modelling the Effect of Water on the Surface Structure and Stability of Forsterite. *Phys. Chem. Miner.* **2000,** *27*, 332-341.

20.   de Leeuw, N. H.; Parker, S. C.; Catlow, C. R. A.; Price, G. D., Proton-Containing Defects at Forsterite {010} Tilt Grain Boundaries and Stepped. *Am. Mineral.* **2000,** *85*, 1143-1154.

21.   de Leeuw, N. H., Density Functional Theory Calculations of Hydrogen-Containing Defects in Forsterite, Periclase, and α-Quartz. *J. Phys. Chem. B* **2001,** *105*, 9747-9754.

22.   Stimpfl, M.; Walker, A. M.; Drake, M. J.; de Leeuw, N. H.; Deymier, P., An Ångström-Sized Window on the Origin of Water in the Inner Solar System: Atomistic Simulation of Adsorption of Water on Olivine. *J. Cryst. Growth* **2006,** *294*, 83-95.

23.   Goumans, T. P. M.; Catlow, C. R. A.; Brown, W. A.; Kastner, J.; Sherwood, P., An Embedded Cluster Study of the Formation of Water on Interstellar Dust Grains. *Phys. Chem. Chem. Phys.* **2009,** *11*, 5431-5436.

24.   de Leeuw, N. H.; Catlow, C. R. A.; King, H. E.; Putnis, A.; Muralidharan, K.; Deymier, P.; Stimpfl, M.; Drake, M. J., Where on Earth Has our Water Come From? *Chem. Commun.* **2010,** *46*, 8923-8925.

25.   King, H. E.; Stimpfl, M.; Deymier, P.; Drake, M. J.; Catlow, C. R. A.; Putnis, A.; de Leeuw, N. H., Computer Simulations of Water Interactions with Low-Coordinated Forsterite Surface Sites: Implications for the Origin of Water in the Inner Solar System. *Earth Planet. Sci. Lett.* **2010,** *300*, 11-18.

26.   Prigiobbe, V.; Suarez Negreira, A.; Wilcox, J., Interaction between Olivine and Water Based on Density Functional Theory Calculations. *J. Phys. Chem. C* **2013,** *117*, 21203-21216.

27.   Asaduzzaman, A. M.; Laref, S.; Deymier, P. A.; Runge, K.; Cheng, H.-P.; Muralidharan, K.; Drake, M. J., A First-Principles Characterization of Water Adsorption on Forsterite Grains. *Phil. Trans. R. Soc. A* **2013,** *371*, 20110582.

28.   Cococcioni, M.; Dal Corso, A.; de Gironcoli, S., Structural, Electronic, and Magnetic Properties of Fe2SiO4 Fayalite: Comparison of LDA and GGA Results. *Phys. Rev. B* **2003,** *67*, 094106.

29.   Lottermoser, W.; Weber, S.-U.; Grodzicki, M.; Kirfel, A.; Amthauer, G., A Semi-Quantitative Approach to Derive the Electric Field Gradient, Applied to Synthetic Fayalite, α-Fe2SiO4: A Reappraisal. *Eur. J. Mineral.* **2012,** *24*, 791-797.

30.   Noël, Y.; De La Pierre, M.; Maschio, L.; Rérat, M.; Zicovich-Wilson, C. M.; Dovesi, R., Electronic Structure, Dielectric Properties and Infrared Vibrational Spectrum of Fayalite: An Ab Initio Simulation with an All-Electron Gaussian Basis Set and the B3LYP Functional. *Int. J. Quantum Chem.* **2012,** *112*, 2098-2108.

31.   Yu, Y. G.; Vinograd, V. L.; Winkler, B.; Wentzcovitch, R. M., Phase Equilibria of (Mg,Fe)2SiO4 at the Earth's Upper Mantle Conditions from First-Principles Studies. *Phys. Earth Planet. Int.* **2013,** *217*, 36-47.

32.   Stucki, W.; Lee, K.; Zhang, L.; Larson, R. A., Effects of Iron Oxidation States on the Surface and Structural Properties of Smectites. *Pure Appl. Chem.* **2002,** *74*, 2145-2158.

33.   Komadel, P.; Madejová, J.; Bujdák, J., Preparation and Properties of Reduced-Charge Smectites - A Review. *Clays Clay Miner.* **2005,** *53*, 313-334.

34.   Stucki, J. W.; Golden, D. C.; Roth, C. B., Effects of Reduction and Reoxidation of Structural Iron on the Surface Charge and Dissolution of Dioctahedral Smectites. *Clays Clay Miner.* **1984,** *32*, 350-356.

35.   Stucki, J. W.; Low, P. F.; Roth, C. B.; Golden, D. C., Effects of Oxidation State of Octahedral Iron on Clay Swelling. *Clays Clay Miner.* **1984,** *32*, 357-362.

36.   Rosso, K. M.; Ilton, E. S., Charge Transport in Micas: The Kinetics of FeII/III Electron Transfer in the Octahedral Sheet. *J. Chem. Phys.* **2003,** *119*, 9207-9218.

37.   Geatches, D. L.; Clark, S. J.; Greenwell, H. C., Iron Reduction in Nontronite-Type Clay Minerals: Modelling a Complex System. *Geochim. Cosmochim. Acta* **2012,** *81*, 13-27.

38.   Geatches, D. L.; Clark, S. J.; Greenwell, H. C., DFT+U Investigation of the Catalytic Properties of Ferruginous Clay. *Am. Mineral.* **2013,** *98*, 132-140.

39.   Alexandrov, V.; Neumann, A.; Scherer, M. M.; Rosso, K. M., Electron Exchange and Conduction in Nontronite from First-Principles. *J. Phys. Chem. C* **2013,** *117*, 2032-2040.

40.   Alexandrov, V.; Rosso, K. M., Insights into the Mechanism of Fe(II) Adsorption and Oxidation at Fe–Clay Mineral Surfaces from First-Principles Calculations. *J. Phys. Chem. C* **2013,** *117*, 22880-22886.

41.   Dovesi, R.; Saunders, V. R.; Roetti, C.; Orlando, R.; Zicovich-Wilson, C. M.; Pascale, F.; Civalleri, B.; Doll, K.; Harrison, N. M.; Bush, I. J., et al., *CRYSTAL09 User's Manual.* University of Torino, Torino, 2009.

42.   Pisani, C.; Dovesi, R.; Roetti, C., *Hartree-Fock Ab Initio Treatment of Crystalline Systems.* Springer-Verlag: Berlin, 1988; Vol. 48.

43.   Noel, Y.; Catti, M.; D'Arco, P.; Dovesi, R., The Vibrational Frequencies of Forsterite Mg2SiO4: An All-Electron Ab Initio Study with the CRYSTAL Code. *Phys. Chem. Miner.* **2006,** *33*, 383-393.

44.   De La Pierre, M.; Orlando, R.; Maschio, L.; Doll, K.; Ugliengo, P.; Dovesi, R., Performance of Six Functionals (LDA, PBE, PBESOL, B3LYP, PBE0, and WC1LYP) in the Simulation of Vibrational and Dielectric Properties of Crystalline Compounds. The Case of Forsterite Mg2SiO4. *J. Comput. Chem.* **2011,** *32*, 1775-1784.

45. De La Pierre, M.; Carteret, C.; Orlando, R.; Dovesi, R., Use of Ab Initio Methods for the Interpretation of the Experimental IR Reflectance Spectra of Crystalline Compounds. *J. Comput. Chem.* **2013,** *34*, 1476-1485.

46. Becke, A. D., Density-functional thermochemistry. III. The role of exact exchange. *The Journal of Chemical Physics* **1993,** *98*, 5648-5652.

47. Lee, C.; Yang, W.; Parr, R. G., Development of the Colle-Salvetti Correlation-Energy Formula into a Functional of the Electron Density. *Phys. Rev. B* **1988,** *37*, 785-789.

48. Broyden, C. G., The Convergence of a Class of Double-Rank Minimization Algorithms. I: General Considerations. *J. Inst. Math. Appl.* **1970,** *6*, 76-90.

49. Fletcher, R., A New Approach to Variable Metric Algorithms. *Comput. J.* **1970,** *13*, 317-322.

50. Goldfarb, D., A Family of Variable-Metric Methods Derived by Variational Means. *Math. Comput.* **1970,** *24*, 23-26.

51. Shanno, D. F., Conditioning of Quasi-Newton Methods for Function Minimization. *Math. Comput.* **1970,** *24*, 647-656.

52. Monkhorst, H. J.; Pack, J. D., Special Points for Brillouin-Zone Integrations. *Phys. Rev. B* **1976,** *13*, 5188-5192.

53. Pascale, F.; Zicovich-Wilson, C. M.; López Gejo, F.; Civalleri, B.; Orlando, R.; Dovesi, R., The Calculation of the Vibrational Frequencies of Crystalline Compounds and its Implementation in the CRYSTAL Code. *J. Comput. Chem.* **2004,** *25*, 888-897.

54. Zicovich-Wilson, C. M.; Dovesi, R.; Saunders, V. R., A General Method to Obtain Well Localized Wannier Functions for Composite Energy Bands in Linear Combination of Atomic Orbital Periodic Calculations. *J. Chem. Phys.* **2001,** *115*, 9708-9719.

55. Zicovich-Wilson, C. M.; Torres, F. J.; Pascale, F.; Valenzano, L.; Orlando, R.; Dovesi, R., Ab Initio Simulation of the IR Spectra of Pyrope, Grossular, and Andradite. *J. Comput. Chem.* **2008,** *29*, 2268-2278.

56. Zicovich-Wilson, C. M.; Bert, A.; Roetti, C.; Dovesi, R.; Saunders, V. R., Characterization of the Electronic Structure of Crystalline Compounds through their Localized Wannier Functions. *J. Chem. Phys.* **2002,** *116*, 1120-1127.

57. Zicovich-Wilson, C. M.; Pascale, F.; Roetti, C.; Saunders, V. R.; Orlando, R.; Dovesi, R., Calculation of the Vibration Frequencies of α-Quartz: The Effect of Hamiltonian and Basis Set. *J. Comput. Chem.* **2004,** *25*, 1873-1881.

58. Ferrero, M.; Rérat, M.; Orlando, R.; Dovesi, R., The Calculation of Static Polarizabilities of 1-3D Periodic Compounds. The Implementation in the Crystal Code. *J. Comput. Chem.* **2008,** *29*, 1450-1459.

59. Ferrero, M.; Rérat, M.; Orlando, R.; Dovesi, R., Coupled Perturbed Hartree-Fock for Periodic Systems: The role of Symmetry and Related Computational Aspects. *J. Chem. Phys.* **2008,** *128*, 014110.

60. Ferrero, M.; Rérat, M.; Kirtman, B.; Dovesi, R., Calculation of First and Second Static Hyperpolarizabilities of One- to Three-Dimensional Periodic Compounds. Implementation in the CRYSTAL Code. *J. Chem. Phys.* **2008,** *129*, 244110.

61. Ferrero, M.; Civalleri, B.; Rérat, M.; Orlando, R.; Dovesi, R., The Calculation of the Static First and Second Susceptibilities of Crystalline Urea: A Comparison of Hartree–Fock and Density Functional Theory Results Obtained with the Periodic Coupled Perturbed Hartree–Fock/Kohn–Sham Scheme. *J. Chem. Phys.* **2009,** *131*, 214704.

62.   Dall'Olio, S.; Dovesi, R.; Resta, R., Spontaneous Polarization as a Berry Phase of the Hartree-Fock Wave Function: The Case of KNbO3. *Phys. Rev. B* **1997,** *56*, 10105-10114.

63.   Baranek, P.; Zicovich-Wilson, C. M.; Roetti, C.; Orlando, R.; Dovesi, R., Well Localized Crystalline Orbitals Obtained from Bloch Functions: The Case of KNbO3. *Phys. Rev. B* **2001,** *64*, 125102.

64.   Noel, Y.; Zicovich-Wilson, C. M.; Civalleri, B.; D'Arco, P.; Dovesi, R., Polarization Properties of ZnO and BeO: An Ab Initio Study through the Berry Phase and Wannier Functions Approaches. *Phys. Rev. B* **2001,** *65*, 014111.

65.   Ferrari, A. M.; Valenzano, L.; Meyer, A.; Orlando, R.; Dovesi, R., Quantum-Mechanical Ab Initio Simulation of the Raman and IR Spectra of Fe3Al2Si3O12 Almandine. *J. Phys. Chem. A* **2009,** *113*, 11289-11294.

66.   Maschio, L.; Ferrabone, M.; Meyer, A.; Garza, J.; Dovesi, R., The Infrared Spectrum of Spessartine: An Ab Initio All Electron Simulation with Five Different Functionals (LDA, PBE, PBESOL, B3LYP and PBE0). *Chem. Phys. Lett.* **2011,** *501*, 612-618.

67.   Dovesi, R.; Pierre, M. D. L.; Ferrari, A. M.; Pascale, F.; Maschio, L.; Zicovich-Wilson, C. M., The IR Vibrational Properties of Six Members of the Garnet Family: A Quantum Mechanical Ab Initio Study. *Am. Mineral.* **2011,** *96*, 1787-1798.

68.   Hazen, R. M., Effects of Temperature and Pressure on Crystal-Structure of Forsterite. *Am. Mineral.* **1976,** *61*, 1280-1293.

69.   Badro, J.; Rueff, J.-P.; Vankó, G.; Monaco, G.; Fiquet, G.; Guyot, F., Electronic Transitions in Perovskite: Possible Nonconvecting Layers in the Lower Mantle. *Science* **2004,** *305*, 383-386.

70.   Tsuchiya, T.; Wentzcovitch, R. M.; da Silva, C. R. S.; de Gironcoli, S., Spin Transition in Magnesiowüstite in Earth's Lower Mantle. *Phys. Rev. Lett.* **2006,** *96*, 198501.

71.   Rouquette, J.; Kantor, I.; McCammon, C. A.; Dmitriev, V.; Dubrovinsky, L. S., High-Pressure Studies of (Mg0.9Fe0.1)2SiO4 Olivine Using Raman Spectroscopy, X-ray Diffraction and Mössbauer Spectroscopy. *Inorg. Chem.* **2008,** *47*, 2668-2673.

72.   Hochella, M. F., Jr., Atomic Structure, Microtopography, Composition and Reactivity of Mineral Surfaces. In *Mineral-water interface geochemistry*, Ribbe, P. H., Ed. Reviews in Mineralogy: Mineralogical Society of America, Washington DC, 1990; Vol. 23, pp 87-132.

73.   de Leeuw, N. H.; Higgins, F. M.; Parker, S. C., Modeling the Surface Structure and Stability of α-Quartz. *J. Phys. Chem. B* **1999,** *103*, 1270-1277.

74.   Servoin, J. L.; Piriou, B., Infrared Reflectivity and Raman Scattering of Mg2SiO4 Single Crystal. *Phys. Status Solid. B* **1973,** *55*, 677-686.

75.   Iishi, K., Lattice Dynamics of Forsterite. *Am. Mineral.* **1978,** *63*, 1198-1208.

76.   Hofmeister, A., Single-Crystal Absorption and Reflection Infrared Spectroscopy of Forsterite and Fayalite. *Phys. Chem. Miner.* **1987,** *14*, 499-513.

77.   Reynard, B., Single-Crystal Infrared Reflectivity of Pure Mg2SiO2 Forsterite and (Mg0.86,Fe0.14)2SiO4 Olivine. *Phys. Chem. Miner.* **1991,** *18*, 19-25.

78.   Chopelas, A., Single Crystal Raman Spectra of Forsterite, Fayalite, and Monticellite. *Am. Mineral.* **1991,** *76*, 1101-1109.

79.   Kolesov, B. A.; Geiger, C. A., A Raman Spectroscopic Study of Fe–Mg Olivines. *Phys. Chem. Miner.* **2004,** *31*, 142-154.

80.   Suto, H.; Sogawa, H.; Tachibana, S.; Koike, C.; Karoji, H.; Tsuchiyama, A.; Chihara, H.; Mizutani, K.; Akedo, J.; Ogiso, K., et al., Low-Temperature Single Crystal Reflection Spectra of Forsterite. *Mon. Not. R. Astron. Soc.* **2006,** *370*, 1599-1606.

81.   Suto, H.; Koike, C.; Sogawa, H.; Tsuchiyama, A.; Chihara, H.; Mizutani, K., Infrared Spectra of Fayalite Crystal. *Astron. Astrophys.* **2002,** *389*, 568-571.
82.   Deer, W. A.; Howie, R. A.; Zussman, J., *An Introduction to the Rock-Forming Minerals*. 2nd ed.; Longman: London, 1992.

Table 1. B3LYP-optimized and experimental bond distance range and cell parameters (in Å) of the bulk structures of Fo, $Fo_{75}{}^{M2}$ and $Fo_{75}{}^{M1}$. The volume of the bulks (in $Å^3$) is also included.

	Fo	Fo, exp	$Fo_{75}{}^{M2}$	$Fo_{75}{}^{M1}$
Si–O	1.628–1.673	1.616–1.649	1.629–1.672	1.633–1.674
Mg1–O	2.073–2.131	2.069–2.126	2.064–2.148	2.096–2.134
Mg2–O	2.062–2.222	2.040–2.166	2.070–2.228	2.066–2.242
Fe1–O	-	-	-	2.119–2.226
Fe2–O	-	-	2.085–2.298	-
a	4.789	4.746	4.791	4.835
b	10.253	10.18	10.369	10.320
c	6.009	5.976	6.063	6.021
Volume	295.10	288.73	301.28	300.46

Table 2. Range of the B3LYP-optimized bond distances of forsterite (Fo^{surf}) and Fe-containing olivine (010) surfaces (Fo_{75}^{top}, Fo_{75}^{mid}, and Fo_{75}^{int}) for the different spin state per Fe^{2+} ion (quintet, qt; triplet, tp; singlet, sg). Values in italics correspond to distances involving atoms present at the outermost positions of the edge-layers.

	Si–O	Mg1–O	Mg2–O	Fe1–O	Fe2–O
Fo^{surf}	1.630–1.703	2.031–2.196	2.052–2.363	–	–
	1.615–1.698	*–*	*1.868–1.912*	*–*	*–*
Fo_{75}^{top}(qt)	1.631–1.703	2.040–2.200	2.071–2.247	–	–
	1.609–1.688	*–*	*–*	*–*	*1.886–1.999*
Fo_{75}^{top}(tp)	1.632–1.703	2.031–2.201	2.061–2.239	–	–
	1.606–1.688	*–*	*–*	*–*	*1.868–1.972*
Fo_{75}^{top}(sg)	1.627–1.705	2.032–2.177	2.070–2.224	–	–
	1.607–1.685	*–*	*–*	*–*	*1.876–1.892*
Fo_{75}^{mid}(qt)	1.638–1.698	2.049–2.178	2.055–2.335	2.062–2.262	–
	1.624–1.696	*–*	*1.863–1.912*	*–*	*–*
Fo_{75}^{mid}(tp)	1.636–1.704	2.025–2.188	2.064–2.398	2.004–2.327	–
	1.627–1.706	*–*	*1.851–1.915*	*–*	*–*
Fo_{75}^{mid}(sg)	1.632–1.698	2.029–2.206	2.063–2.314	2.035–2.173	–
	1.617–1.698	*–*	*1.863–1.912*	*–*	*–*
Fo_{75}^{int}(qt)	1.628–1.701	2.026–2.213	–	–	2.103–2.471
	1.617–1.701	*–*	*1.874–1.925*	*–*	*–*
Fo_{75}^{int}(tp)	1.631–1.703	2.042–2.184	–	–	2.023–2.419
	1.615–1.704	*–*	*1.873–1.918*	*–*	*–*
Fo_{75}^{int}(sg)	1.632–1.699	2.031–2.174	–	–	2.070–2.155
	1.611–1.699	*–*	*1.864–1.906*	*–*	*–*

Table 3. B3LYP-optimized cell parameters of forsterite (Fo^{surf}) and Fe-containing olivine (010) surfaces (Fo_{75}^{top}, Fo_{75}^{mid}, and Fo_{75}^{int}) for the different spin state per Fe^{2+} ion (quintet, qt; triplet, tp; singlet, sg). Surface areas (in $Å^2$) and calculated surface energies (Jm^{-2}) are included.

	a	c	Area	E_{surf}
Fo^{surf}	4.831	6.141	29.67	1.160
$Fo_{75}^{top}(qt)$	4.817	6.153	29.65	0.870
$Fo_{75}^{top}(tp)$	4.805	6.176	29.68	1.538
$Fo_{75}^{top}(sg)$	4.809	6.016	28.94	2.201
$Fo_{75}^{int}(qt)$	4.875	6.163	30.05	1.111
$Fo_{75}^{int}(tp)$	4.830	6.102	29.48	1.644
$Fo_{75}^{int}(sg)$	4.813	6.128	29.50	1.709
$Fo_{75}^{ins}(qt)$	4.839	6.203	30.02	1.097
$Fo_{75}^{ins}(tp)$	4.836	6.197	29.97	1.768
$Fo_{75}^{ins}(sg)$	4.807	6.107	29.36	2.039

Table 4. Comparison of the B3LYP vibrations (cm^{-1}) with the experimental ones for the bulk forsterite. "Represented IR bands" refers to those bands shown in Figure 5. Calculated intensities (values in brackets) are in km mol^{-1}. Assignment of the vibration symmetry is also included.

Represented IR Band	Vibrations			
	B3LYP	[Intensity]	Experimental	Symmetry
293	291	[673.52]	291	B_{3u}
	294	[806.38]	293	B_{1u}
	295	[223.87]	296	B_{2u}
350	350	[1035.69]	352	B_{3u}
389	389	[1059.96]	383	B_{2u}
	404	[269.18]	397	B_{3u}
416	412	[1288.46]	412	B_{1u}
	420	[985.05]	419	B_{1u}
	421	[31.42]	420	B_{3u}
514	513	[527.73]	505	B_{2u}
	514	[641.76]	506	B_{1u}
	517	[74.45]	508	B_{3u}
614	614	[463.53]	606	B_{2u}
873	870	[1561.67]	873	B_{3u}
	874	[2659.78]	874	B_{1u}
982	982	[1413.29]	978	B_{2u}
	989	[43.58]	987	B_{3u}

Table 5. B3LYP-calculated high frequency dielectric constants (ε_∞) for the bulk systems of Fo and Fo_{75}^{M2} along the x, y and z directions. Experimental (Exp.) values for the olivine end-members Mg_2SiO4 and Fe_2SiO_4 are also included (from ref. [82])

	Mg_2SiO_4			$(Mg_{1.5},Fe_{0.5})SiO_4$	Fe_2SiO_4
	Fo/B3LYP	Exp.	Deviation (%)	Fo_{75}^{M2}/B3LYP	Exp.
$\varepsilon_{\infty,x}$	2.571	2.789	-7.8	2.715	3.55
$\varepsilon_{\infty,y}$	2.424	2.673	-9.3	2.592	3.35
$\varepsilon_{\infty,z}$	2.475	2.726	-9.2	2.671	3.50
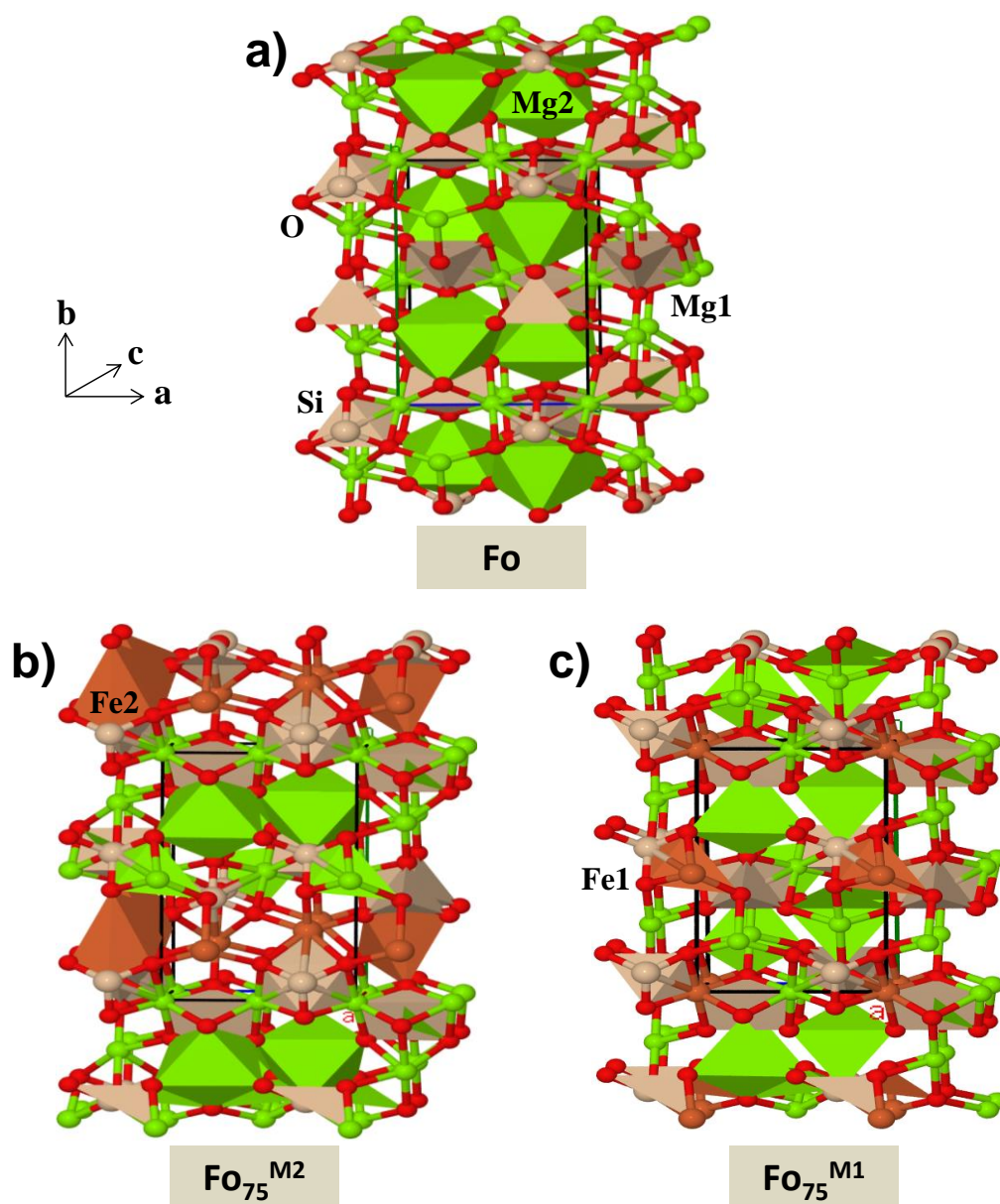
Figure 1. View (along the c crystallographic axis) of the crystal structure of forsterite (Fo, a) and $Mg_{1.5}Fe_{0.5}SiO_4$, in which Fe^{2+} occupies the M2 position (Fo_{75}^{M2}, b) and the M1 position (Fo_{75}^{M1}, c).
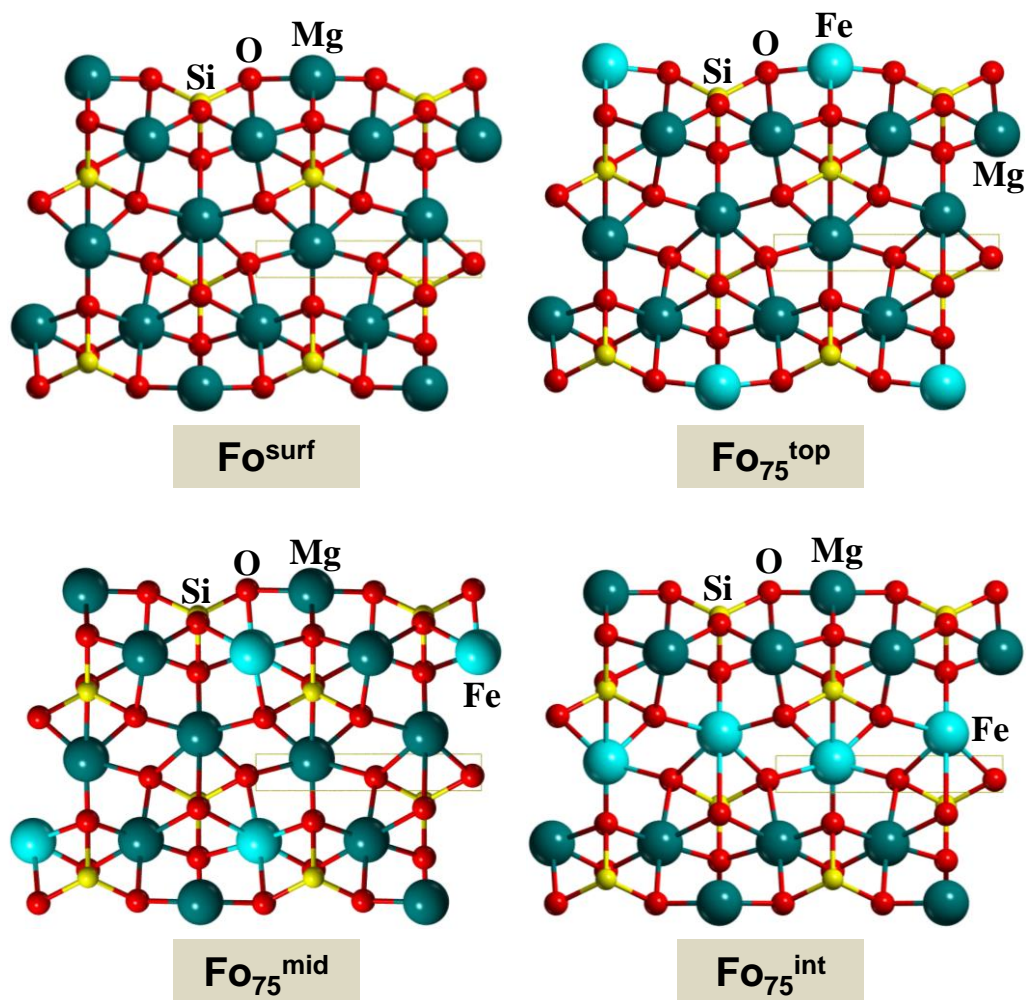
Figure 2. Lateral views of the non-polar (010) surfaces for forsterite (Fo^{surf}) and for the Fe-containing olivine surfaces (Fo$_{75}^{top}$, Fo$_{75}^{mid}$ and Fo$_{75}^{int}$).
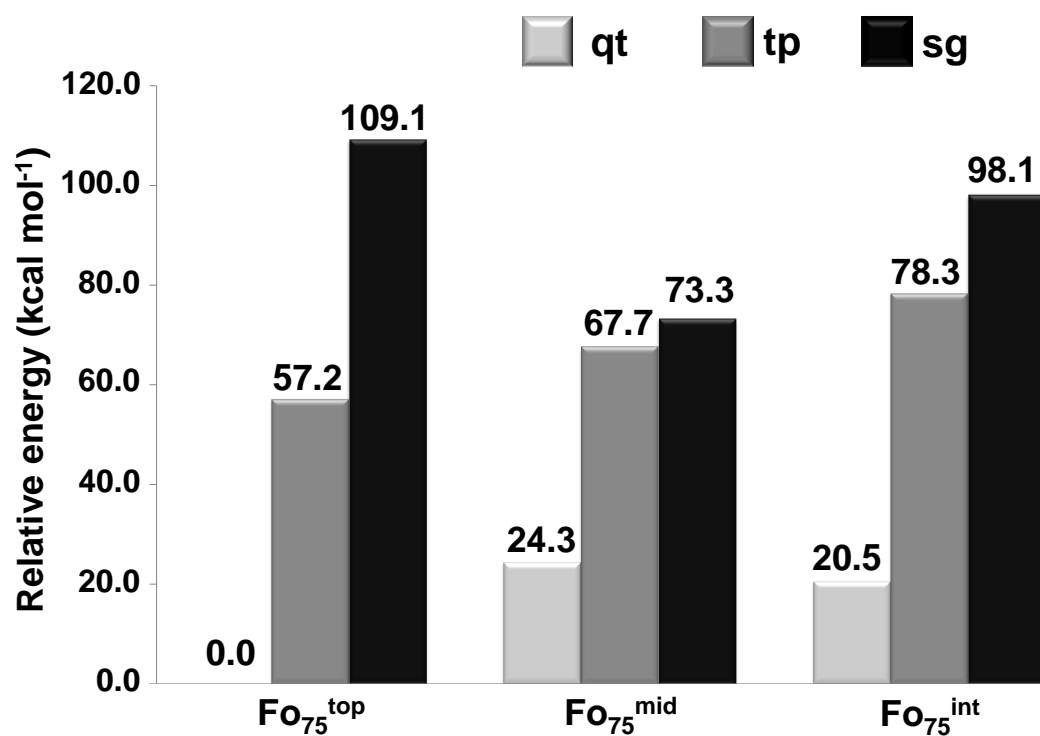
Figure 3. Relative stability of the non-polar (010) Fe-containing surfaces as a function of the spin configuration per Fe^{2+} ion (quintet, qt; triplet, tp; singlet, sg) and the position of the Fe^{2+} ions in the slab models.
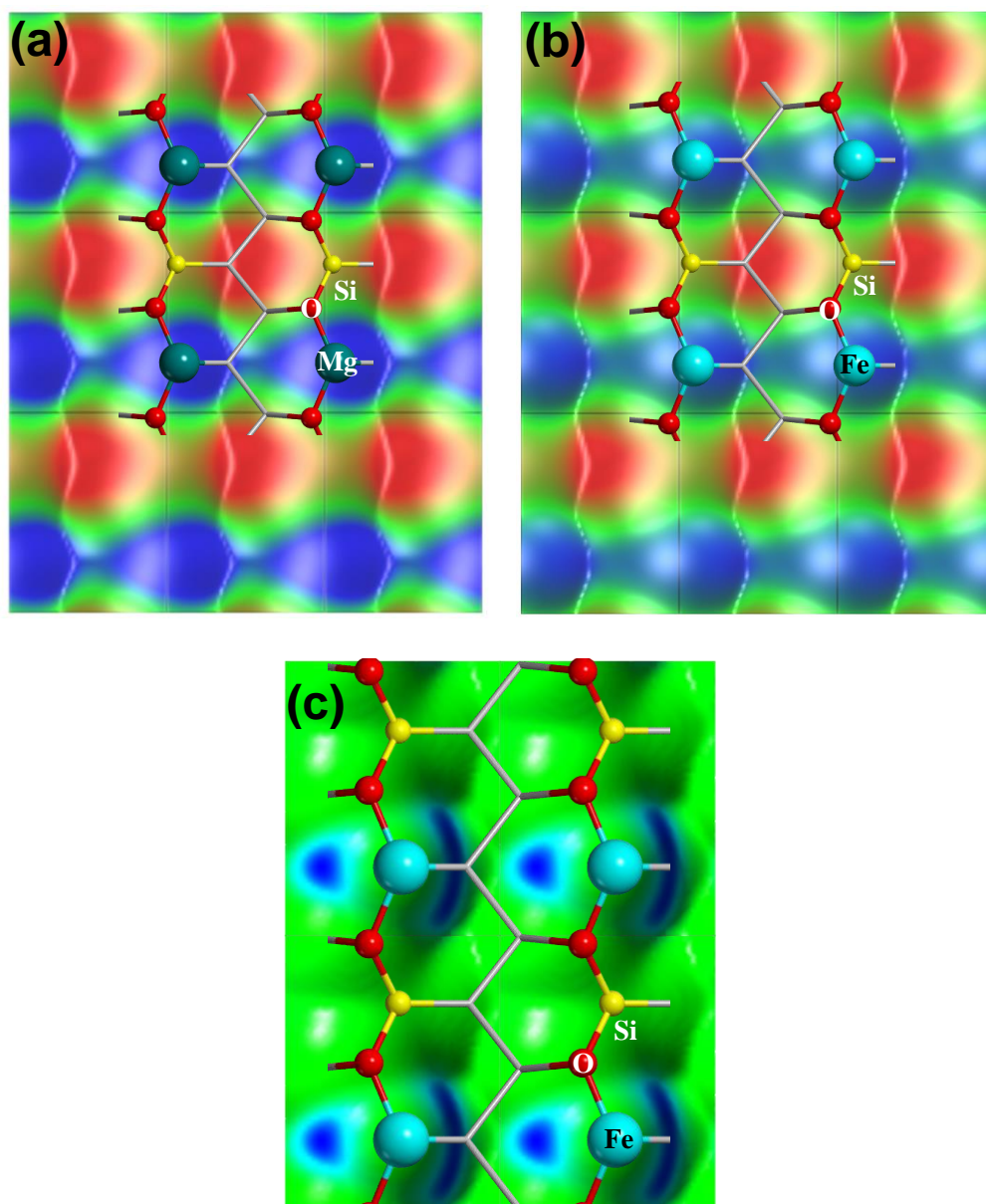
Figure 4. Top views of the electrostatic potential maps of the Fo^{surf} (a) and $Fo_{75}^{top}(qt)$ (b) slab models and of the spin density map of the $Fo_{75}^{top}(qt)$ surface (c) mapped on surfaces enclosing 90% of the total electron density. Negative values (-0.02 a.u.) coded as red colors; positive values (+0.02 a.u.) coded as blue colors; green color indicates ≈ 0.0 a.u. electrostatic potential values or spin density values.

Fo bands (cm^{-1})	Fo$_{75}^{M2}$ bands (cm^{-1})	Vibrational Mode
293	276	Transl. Mg (+ Fe)
350	280	Transl. Mg (+ Fe)
389	373	Rot. SiO$_4$
416	406	Rot. SiO$_4$
514	513	Bending SiO$_4$
614	603	Bending SiO$_4$
873	855	Stretching SiO$_4$
982	978	Stretching SiO$_4$
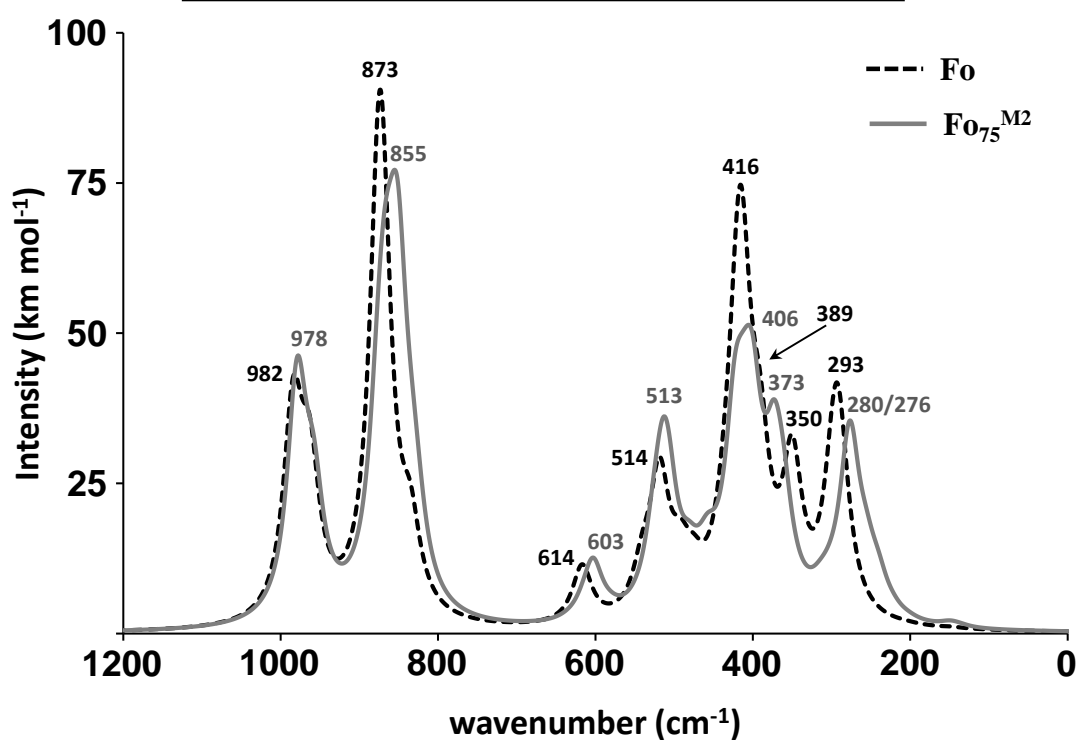
Figure 5. B3LYP-simulated infrared spectra of the Fo (dashed-black) and Fo$_{75}^{M2}$ (solid-grey) bulk structures. Shift range with respect to the experimental values (ref. [80]) are also included

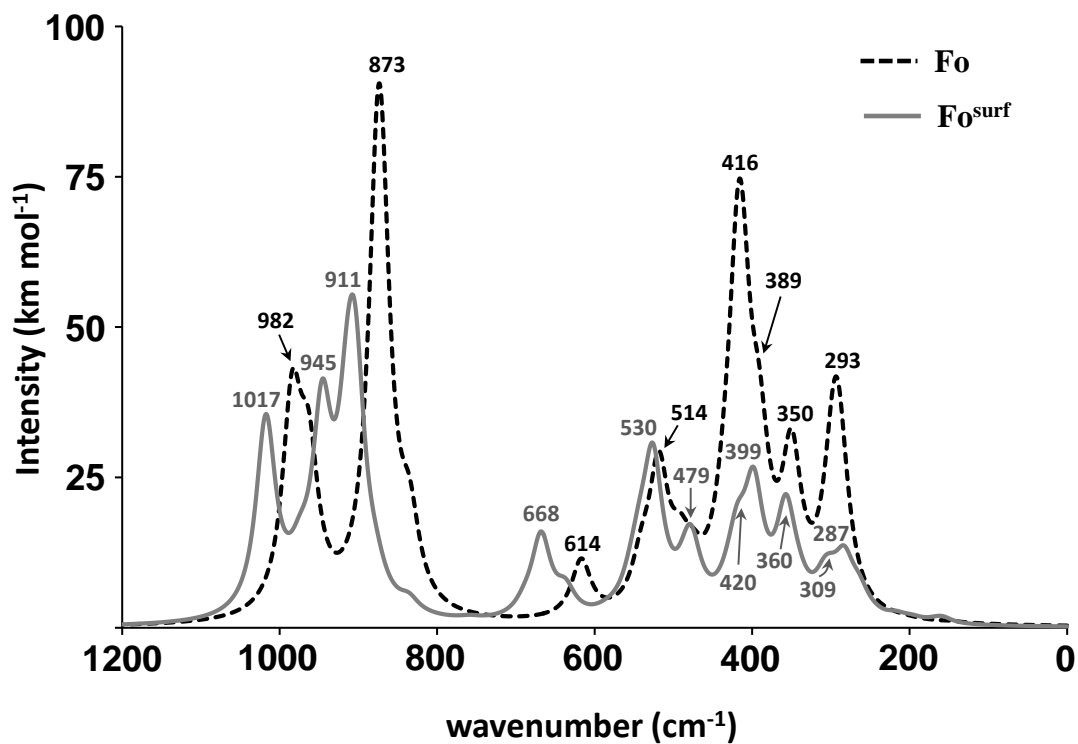| Fo bands (cm⁻¹)	Fo^surf bands (cm⁻¹)	Vibrational Mode
293/350	287/309/360	Transl. Mg
389/416	399/420	Rot. SiO_4
514/614	479/530/668	Bending SiO_4
873/982	911/945/1017	Stretching SiO_4

Figure 6. B3LYP-simulated infrared spectra of the Fo bulk structure (dashed-black) and Fo^surf non-polar (010) surface (solid-grey).

Fo$_{75}^{M2}$ bands (cm^{-1})	Fo$_{75}^{top}$(qt) bands (cm^{-1})	Vibrational Mode
280/276	279/304/348	Transl. Mg (+ Fe)
373/406	372/407	Rot. SiO$_4$
513/603	468/504/624	Bending SiO$_4$
855/978	892/920/1023	Stretching SiO$_4$
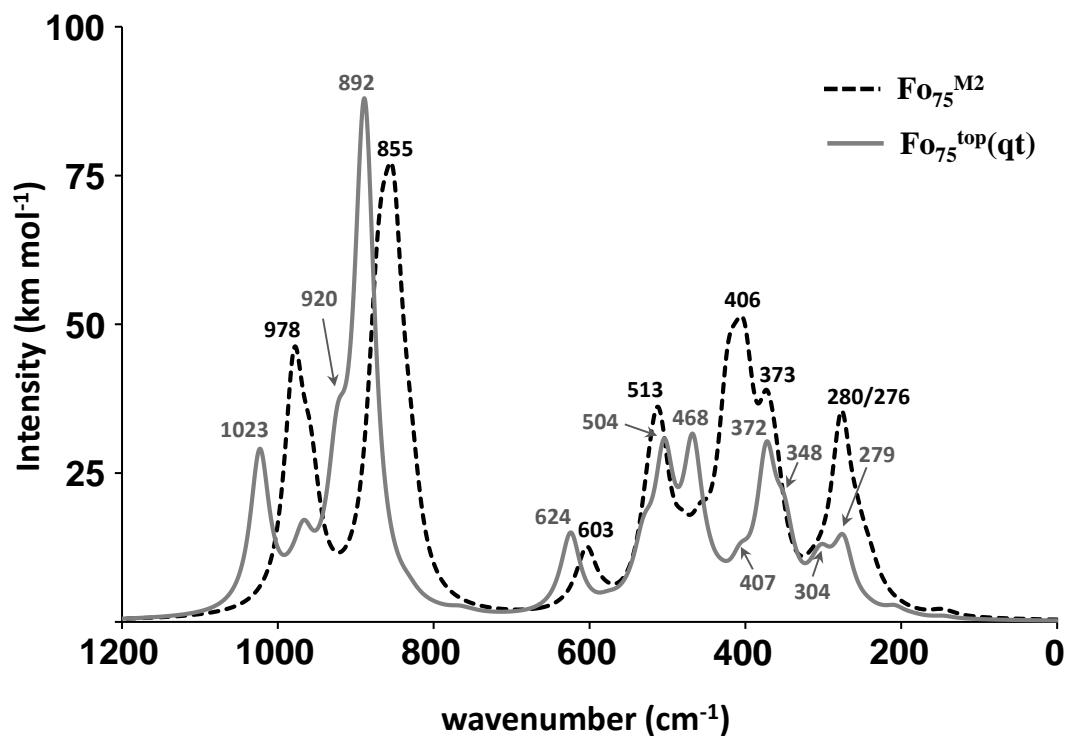
Figure 7. B3LYP-simulated infrared spectra of the Fo$_{75}^{M2}$ bulk structure (dashed-black) and Fo$_{75}^{top}$(qt) non-polar (010) surface (solid-grey).
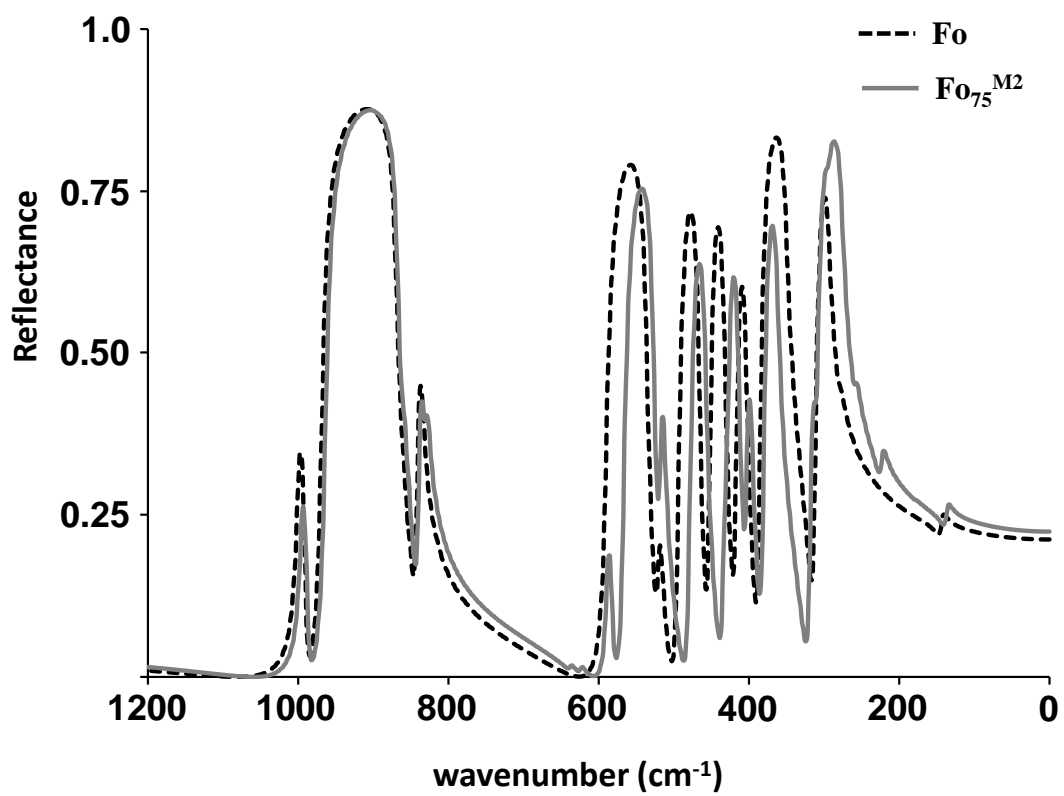
Figure 8. B3LYP-simulated reflectance spectra of the Fo (dashed-black) and Fo_{75}^{M2} (solid-grey) bulk structures.

Graphical Abstract of

B3LYP Periodic Study of the Physico-Chemical Properties of the Non-Polar (010) Mg-Pure and Fe-Containing Olivine Surfaces

Javier Navarro-Ruiz,[a] Piero Ugliengo,[b] Albert Rimola[a,*] and Mariona Sodupe[a,*]